Parameter fitting-based traveling wave fault location method for multi-terminal DC grids

Liu, Le; Xie, Fan; Kang, Xiaoning; Hao, Zhiguo; Lekić, Aleksandra; Popov, Marjan

DOI
10.1016/j.ijepes.2024.110412

Publication date
2025

Document Version
Final published version

Published in
International Journal of Electrical Power and Energy Systems

Citation (APA)
Liu, L., Xie, F., Kang, X., Hao, Z., Lekić, A., & Popov, M. (2025). Parameter fitting-based traveling wave fault location method for multi-terminal DC grids. *International Journal of Electrical Power and Energy Systems*, *164*, Article 110412. https://doi.org/10.1016/j.ijepes.2024.110412

Electrical Power and Energy Systems 164 (2025) 110412

Contents lists available at ScienceDirect

International Journal of Electrical Power and Energy Systems

journal homepage: www.elsevier.com/locate/ijepes

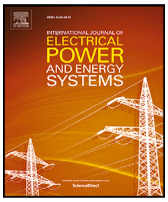

Parameter fitting-based traveling wave fault location method for multi-terminal DC grids[☆]

Le Liu [a,b,*,1], Fan Xie [a,b,c,1], Xiaoning Kang [a], Zhiguo Hao [a], Aleksandra Lekić [b], Marjan Popov [b]

[a] School of Electrical Engineering, Xi'an Jiaotong University, Xi'an, 710049, China
[b] Faculty of Electrical Engineering, Mathematics and Computer Science, Delft University of Technology, Delft, 2628 CD, The Netherlands
[c] Electric Power Research Institute, China Southern Power Grid, Guangzhou, 510663, China

ARTICLE INFO

Keywords:
MTDC
Fault location
Traveling wave
Parameter fitting
Adaptive multi-step Levenberg–Marquardt algorithm
RTDS

ABSTRACT

DC fault location technology is crucial for estimating the fault location and developing multi-terminal direct current (MTDC) systems. This article presents a novel fault location method using the parameter fitting approach. The propagation of traveling waves (TWs) in the decoupled line-mode fault network is first discussed, resulting in analytical expressions for the backward line-mode current TWs containing fault location information. Then, the adaptive multi-step Levenberg–Marquardt (AMLM) algorithm is applied for parameter fitting owing to its fast processing speed and precision. The exact fault location is estimated using the fitted coefficient. Different testing MTDC systems modeled in PSCAD/EMTDC and a real-time digital simulator (RTDS) validate the proposed fault location method. Based on numerous simulation tests, the AMLM-based parameter fitting and the proposed method are accurate, with errors smaller than 0.5%. Compared to the existing methods, the proposed method has desired performance under close-in faults, can withstand 35 dB noise interference, and obviates the need for an extremely high sampling frequency, estimation of tws velocity, and communication devices.

1. Introduction

The modular multilevel converter (MMC)-based HVDC transmission systems are widely recognized as the most efficient and cost-effective solutions for interconnecting separate national or regional grids. They are frequently utilized to link fluctuating offshore wind farms and transmit electricity over extended distances. Notable examples include the Zhangbei, and Zhoushan multi-terminal HVDC (MTDC) grids in China [1] and the BorWin, DolWin, and NorNed offshore HVDC projects in the North Sea.

Unpredictable different DC faults can occur at any location along the HVDC transmission line. In the case of a DC fault, DC voltage can drop considerably, and the fault current will swiftly increase to its peak value in just a few milliseconds. Such a contingency can damage the power electronics (e.g., IGBTs) and lead to a complete system collapse and power outage [2]. To mitigate this risk, it is crucial to develop methods for detecting DC faults, clearing faults, locating faults, and recovering from faults to ensure continuous operation and stability in MTDC systems. Among these critical elements, an accurate DC fault location technique is important for system operators, which would significantly minimize electricity loss, and fasten the fault section repair and system restoration process.

1.1. Related works

Many researchers have developed numerous methods to cope with the problem of fault location. The natural frequency-based methods aim to establish the mapping relationship between natural frequency, fault location, and reflection coefficients. The natural frequencies contained in post-fault voltages/currents can be obtained using the MUSIC or PRONY algorithm [3,4]. These frequencies are then utilized to calculate the velocity of the TWs and the reflection coefficient for estimating the fault location. Generally, these methods require a very high sampling frequency (e.g., 10 MHz as cited in [3]) and fail to accurately determine the fault location when the fault is near the line terminal, that is to say, a dead zone may exist. Additionally, the performance of these methods heavily depends on the accurate values of line parameters [3],

---

[☆] This work was supported by the Young Scientists Fund of the National Natural Science Foundation of China (Grant No. 52407142).

[*] Corresponding author at: School of Electrical Engineering, Xi'an Jiaotong University, Xi'an, 710049, China.

E-mail addresses: liule@xjtu.edu.cn (L. Liu), xiefan@csg.cn (F. Xie), Kangxn@xjtu.edu.cn (X. Kang), zhghao@mail.xjtu.edu.cn (Z. Hao), A.Lekic@tudelft.nl (A. Lekić), M.Popov@tudelft.nl (M. Popov).

[1] L. Liu and F. Xie are co-first authors. L. Liu is the corresponding author (liule@xjtu.edu.cn).

https://doi.org/10.1016/j.ijepes.2024.110412
Received 8 July 2024; Received in revised form 12 October 2024; Accepted 2 December 2024

the system structure, physical boundary conditions, and the precision of the natural frequency extraction method. Furthermore, in the case of asymmetrical faults, cross-coupled line- and zero-mode signals can cause aliasing problems in the measured natural frequency.

The time-domain analysis-based methods calculate the voltage/current expressions at any point and then locate the fault using the fault characteristics of measured voltages/currents. The authors in [5] proposed a simplified $R-L$ representation to model a detailed frequency-dependent transmission line by calculating the $R-L$ parameters for fault location. In [6], the voltage distribution along the cable is calculated using voltages and currents based on the numerical Laplace transform (NLT). Then, the cable parameter suitable for the NLT is combined with the multiround iteration (MRI) algorithm for fault location purposes. Compared to natural frequency-based methods, these methods do not require a very high sampling frequency. However, they rely on an aggregated transmission line model, and the accuracy of these fault analysis methods is not guaranteed when applied to long transmission lines with frequency-dependent characteristics.

The active injection-based methods in [7,8] will actively inject a specific detecting signal at the line terminal, and the characteristics of the reflected signals from the fault point are utilized to calculate the fault location. However, an additional device or a control loop for signal injection is generally required. The timing, signal type, and mechanism of the signal injection must be specifically designed for the applied system, which causes additional burden and cost, and reduces the adaptability of these methods. Moreover, the accuracy of these methods can be affected by fault resistance and the size of the DC inductor.

The AI-based methods discussed in [9–11] focus on preprocessing extensive fault data and training AI models to estimate fault locations. In [9], a set of profiles of the difference between the 1-mode and 0-mode voltages are used as inputs for the artificial neural network (ANN). Empirical mode decomposition (EMD) is employed in [10] to decompose fault signals into intrinsic mode functions (IMFs), which are then used to train a convolutional neural network (CNN) for fault location. The approach in [11] uses discrete wavelet transform (DWT) to decompose the current signals, the detailed and approximate components are feed into an ANFIS-based fault model for fault detection and localization. However, these AI-based methods require a lot of input data and samples (e.g., 2190 input vectors in [10]). Various fault conditions, including fault types, locations, and associated resistances, must be simulated to build a comprehensive fault data library. These data need to be processed using tools like VMD and DWT to obtain additional fault features as input, which causes an extremely high computational burden. Besides, such fault data can be generated in simulation environments like PSCAD/EMTDC. However, collecting such fault data sets via real DC faults for the AI model training in practice is not realistic. Moreover, the complexity of model design, such as network architecture, neuron count, network model, and required sampling data, which poses further challenges for adapting these methods to other systems.

Due to the above limitations, the aforementioned methods are still at the theoretical and simulation testing stage, and the practical application needs further research.

Traveling wave-based fault location methods are simple and easy to implement in reality and have the advantage of high precision, which is widely applied in real environments. There are two categories of TW-based methods: single-ended and double-ended. The authors in [12] utilize the least squares error (LSE) algorithm to analyze the low-frequency components in voltage/current traveling waves (TWs) from both terminals to locate the faults. Similar research can be also found in [13,14]. However, these methods have inherent shortcomings. For example, the measured TWs signals at different relays and measuring units must be synchronized, and the reliability and accuracy can be affected by communication interruption, data damage or loss, and synchronization errors. The single-ended methods eliminate the need for data synchronization. The fault location is determined based on the time interval between two consecutive wavefronts of the fault-induced TWs using different time–frequency analyzing tools, including the Successive Variational Mode Decomposition (SVMD) Teager Energy Operator (TEO) and Modified Variational Mode Decomposition (MVMD)-TEO [15,16], the S- transform and stationary wavelet transform (SWT) [17,18], etc.

1.2. Motivation and main contributions

Despite the several advances in the existing TWs-based methods, the following aspects of limitations are exposed:

- the need for an extremely high sampling frequency to detect the wavefronts/turning points to determine the TW’s arrival time;
- the reduced accuracy and reliability under close-in faults;
- the need for precise calculation of the TWs propagation velocity;
- the non-independence to the boundary and fault conditions;

In this context, this article proposes a parameter fitting-based fault location method. Compared with the existing fault location methods, the novelty and the main contributions of our research are threefold. Firstly, the proposed method provides a new perspective on fault location in MTDC systems. It uses the fitted coefficients of the Backward Line-mode Current TWs (BLCTWs) to estimate the fault location, eliminating the need to estimate the TWs velocity. Secondly, the proposed fault location method does not require an extremely high sampling frequency to detect the refraction/reflection time of TWs. This significantly reduces hardware requirements and investment in practical applications and guarantees fault location accuracy. Thirdly, compared to existing methods, the fault location accuracy is independent of the size of the DC inductor, noise disturbance, and sampling frequency and is robust to close-in faults.

The rest of the paper is organized as follows. Section 2 outlines the testing system setups in PSCAD/EMTDC. Section 3 presents the theoretical analysis of the backward line-mode current traveling waves after a DC fault. Section 4 describes the proposed fault location method using AMLM-based parameter fitting. Section 5 validates the performance of the fault location in the PSCAD environment. Section 6 provides the RTDS simulation conditions and the corresponding experimental test results. Finally, conclusions are elaborated in Section 7, which also refers to future work.

2. Test system in PSCAD

The four-terminal MMC-based HVDC system depicted in Fig. 1 is modeled in the PSCAD/EMTDC environment, following the CIGRE benchmarked testing model DCS2 (B4.57 working group) [19]. The DC voltage level has been adjusted to a ±320 kV rating. The AC grids labeled G_1 to G_4, operate at a rated frequency of 50 Hz. The DC buses are denoted by M, N, P, and Q. Each cable is equipped with a 40 mH DC inductor (L_{dc}) at the end to limit the rate of rise and the peak value of the fault current.

In Fig. 1, four MMC converters are connected using frequency-dependent (phase) cables ($l_{12}-l_{34}$) with a distance of 200 km. The practical cable line is modeled with frequency-dependent distributed parameters. Such a cable model can accurately take into account the high-frequency transient response of traveling waves along a long distance. The detailed cable model adopted can be seen in Fig. 2. At each end of the DC cable, two relay units R_{ij} and R_{ji} are installed on the positive and negative poles to measure the current/voltage signals, the subscript $i,j\in\{1,2,3,4\}$ denotes the connections of MMCs to the DC cables. The focus of this paper is estimating the precision fault location in the faulty section. The DC protection in the studied system uses the protection algorithm developed in [20], and all thresholds have been adjusted to this testing system. The fault current interruption using the VSC-assisted resonant current (VARC) DCCBs following the approach presented in [21]. The system and MMC parameters are listed in the Table 1.

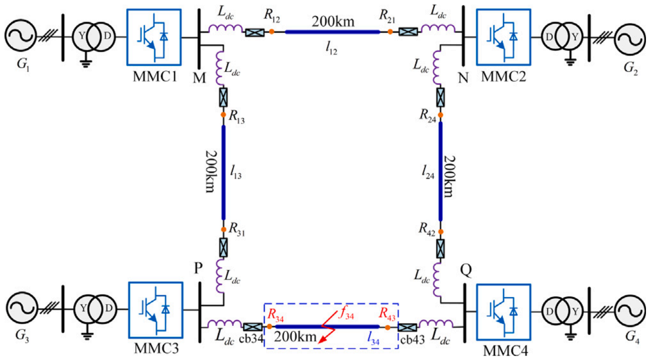

Fig. 1. Structure of the studied four-terminal MMC-based HVDC system.

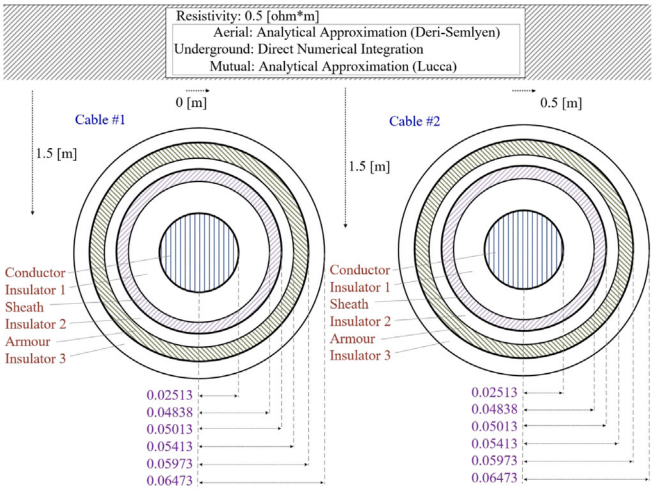

Fig. 2. The configuration of frequency-dependent cable model.

Table 1
Detailed parameters of the testing system.

Items	MMC1&4	MMC2	MMC3
Rated capacity	1500 MVA	1500 MVA	1500 MVA
DC link voltage	±320 kV	±320 kV	±320 kV
SMs number per arm (N)	200	200	200
Arm capacitance (C_{sm})	15 000 μF	15 000 μF	15 000 μF
Arm inductance (L_{arm})	5 mH	5 mH	5 mH
DC inductance (L_{dc})	40 mH	40 mH	40 mH
IGBT on-state (R_{on})	1.361 mΩ	5.445 mΩ	0.908 mΩ

3. Time-domain expression analysis of the backward line-mode current traveling wave

The parameters of time-domain expressions of Backward line-mode current TWs are independently mapped to the fault location and thus can be used for fault location. This section aims to derive detailed expressions of BLCTWs after typical DC faults in the MTDC systems.

3.1. Pre-data processing

The following modal transform is used to eliminate the mutual coupling effect of the bipolar transmission line:

$$\begin{bmatrix} A_0 \\ A_1 \end{bmatrix} = \frac{1}{\sqrt{2}} \begin{bmatrix} 1 & 1 \\ 1 & -1 \end{bmatrix} \begin{bmatrix} A_p \\ A_n \end{bmatrix} \tag{1}$$

where $A_{0,1}$ represents the decoupled line- and zero-mode DC voltage/current components. $A_{p,n}$ refers to measured positive and negative pole voltage/current components.

Table 2
Line- and zero-mode initial voltages at fault point [20].

Item	ptp	ptg	ntg
Δv_{F1}	$\frac{-\sqrt{2}V_f Z_{c(1)}}{Z_{c(1)}+R_f}$	$\frac{-\sqrt{2}V_f Z_{c(1)}}{Z_{c(1)}+Z_{c(0)}+4R_f}$	$\frac{-\sqrt{2}V_f Z_{c(1)}}{Z_{c(1)}+Z_{c(0)}+4R_f}$
Δv_{F0}	0	$\frac{-\sqrt{2}V_f Z_{c(0)}}{Z_{c(1)}+Z_{c(0)}+4R_f}$	$\frac{\sqrt{2}V_f Z_{c(0)}}{Z_{c(1)}+Z_{c(0)}+4R_f}$

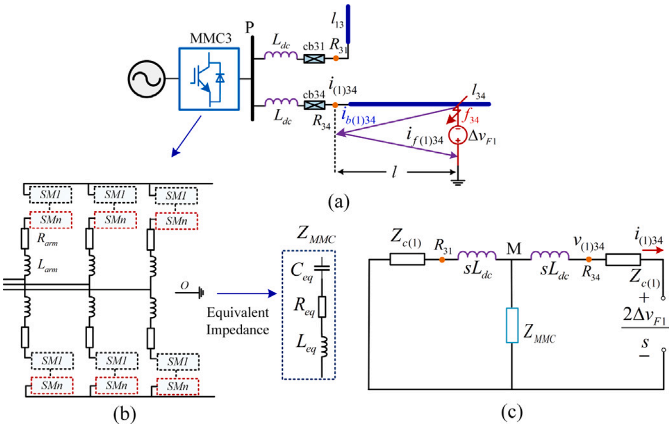

Fig. 3. (a) Fault f_{34} in the line-mode network. (b) MMC equivalent impedance. (c) Line-mode fault component *Peterson* equivalent circuit.

3.2. The time-domain expressions of line-mode current TWs

The initial values of the line-mode voltage at the fault point Δv_{F1} for a typical pole-to-pole (ptp) fault, positive pole-to-ground (ptg) fault, and negative pole-to-ground (ntg) fault can be obtained using the fault sequence networks, and are summarized in Table 2.

In Table 2, V_f denotes the rated line voltage, R_f refers to the fault resistance, $Z_{c(1)}$ and $Z_{c(0)}$ represent the line- and zero-mode characteristic impedances, respectively. According to Table 2, the initial value of Δv_{F0} is zero for the ptp faults, indicating that the zero-mode TWs are unsuitable for fault location analysis as they cannot reflect all types of fault information. Therefore, the line-mode components generated by Δv_{F1} are considered for analyzing the TWs propagation in the following analysis.

We selected cable l_{34} as the faulty cable and thus the relay units R_{34} and R_{43} as the observed relays. Fig. 3(a) describes the diagram for an internal DC fault f_{34} in the line-mode network. Fig. 3(b) denotes the equivalent impedance of MMC converter; Fig. 3(c) presents the line-mode fault component *Peterson* equivalent circuit [20].

As shown in Fig. 3(b), Z_{MMC} represents the equivalent impedance of the MMC converter, which is generally considered a series *RLC* circuit [20]: $R_{eq} = \frac{2}{3}(R_{arm} + R_{on})$, $L_{eq} = \frac{2}{3}L_{arm}$, and $C_{eq} = \frac{6C_{sm}}{N}$. Here, R_{eq}, L_{eq}, and C_{eq} are the equivalent resistance, inductance, and capacitance of the MMC, respectively. For the adopted MMC model, we have $R_{eq} = 0.907$ mΩ, $C_{eq} = 0.45 \times 10^3$ μF, and $L_{eq} = 3.33$ mH. To simplify the subsequent analysis, $Z_{MMC}(s) \approx 1/(sC_{eq}) + sL_{eq}$, as the impact of R_{eq} is negligible.

According to the *Peterson* rule, the voltage source in the equivalent *Peterson* circuit equals twice the voltage at the fault point. As such, one can obtain the *Laplace*-domain expression for line-mode current $i_{(1)34}(s)$ and voltage $v_{(1)34}(s)$ using the circuit Fig. 3(c):

$$\begin{cases} i_{(1)34}(s) = \dfrac{2\Delta v_{F1}}{s}\dfrac{1}{Z_{c(1)}+sL_{dc}+Z_P} \\ \quad = \dfrac{2\Delta v_{F1}}{s}\dfrac{(s-z_1)(s-z_2)}{(Z_{c(1)}+sL_{dc})(s-p_1)(s-p_2)}, \\ v_{(1)34}(s) = \dfrac{2\Delta v_{F1}}{s}\left(1-\dfrac{Z_{c(1)}}{Z_{c(1)}+sL_{dc}+Z_P}\right) \\ \quad = \dfrac{2\Delta v_{F1}}{s}\left(1-\dfrac{Z_{c(1)}(s-z_1)(s-z_2)}{(Z_{c(1)}+sL_{dc})(s-p_1)(s-p_2)}\right). \end{cases} \tag{2}$$

where z_1, z_2, p_1, p_2, and Z_P in (2) are calculated by:

$$\begin{cases} z_{1,2} = \dfrac{-Z_{c(1)}C_{eq} \pm \sqrt{(Z_{c(1)}C_{eq})^2 - 4C_{eq}(L_{dc}+L_{eq})}}{2C_{eq}(L_{dc}+L_{eq})}, \\ p_{1,2} = \dfrac{-Z_{c(1)}C_{eq} \pm \sqrt{(Z_{c(1)}C_{eq})^2 - 8C_{eq}(L_{dc}+2L_{eq})}}{2C_{eq}(L_{dc}+2L_{eq})}, \\ Z_P = \dfrac{(Z_{c(1)}+sL_{dc})(\frac{1}{sC_{eq}}+sL_{eq})}{Z_{c(1)}+sL_{dc}+\frac{1}{sC_{eq}}+sL_{eq}}. \end{cases} \tag{3}$$

Given that the $L_{dc} = 40$ mH, and the line-mode characteristic impedance is $Z_{c(1)} = 19.0\ \Omega$, one can obtain that: $Z^2_{c(1)}C^2_{eq} = 73.10\times10^6 \gg 8C_{eq}(2L_{eq}+L_{dc}) = 167.97\times10^3 > 4C_{eq}(L_{dc}+L_{eq}) = 77.99\times10^3$. Given these values, we can simply the roots in (3) as follows: $z_1 = p_1 \approx 0$, $z_2 \approx -Z_{c(1)}/(L_{dc}+L_{eq})$, and $p_2 \approx -Z_{c(1)}/(L_{dc}+2L_{eq})$. if we further consider that $L_{dc}+L_{eq} = 43.33$ mH $\approx L_{dc}+2L_{eq} = 46.66$ mH, we have:

$$\begin{cases} i_{(1)34}(s) = \dfrac{2\Delta v_{F1}}{s}\cdot\dfrac{1}{Z_{c(1)}+sL_{dc}}, \\ v_{(1)34}(s) = \dfrac{2\Delta v_{F1}}{s}\cdot\dfrac{sL_{dc}}{Z_{c(1)}+sL_{dc}}. \end{cases} \tag{4}$$

To describe the attenuation effect of line-mode TWs along the traveling distance l and the velocity $v_{(1)}$ in the cable, the $i_{(1)34}(s)$ and $u_{(1)34}(s)$ in (4) can be further extended as [20]:

$$\begin{cases} i_{(1)34}(s) = \dfrac{2\Delta v_{F1}}{s}\dfrac{1}{Z_{c(1)}+sL_{dc}}\dfrac{1-kl}{1+s\tau l}\cdot \mathrm{e}^{-s\frac{l}{v_{(1)}}} \\ v_{(1)34}(s) = \dfrac{2\Delta v_{F1}}{s}\dfrac{sL_{dc}}{Z_{c(1)}+sL_{dc}}\dfrac{1-kl}{1+s\tau l}\,\mathrm{e}^{-s\frac{l}{v_{(1)}}} \end{cases} \tag{5}$$

To this end, we have obtained the detailed S-domain expressions of $i_{(1)34}(s)$ and $u_{(1)34}(s)$, and the time-domain expressions can be achieved by using the *Inverse Laplace Transform* of (5). However, using the line-mode components will increase complexity and data-analyzing load as the time-domain expressions of $i_{(1)34}(t)$ and $u_{(1)34}(t)$ are complex. The parameters of $i_{(1)34}(t)$ and $u_{(1)34}(t)$ are not independently mapped to the fault location due to the injections/reflections at the DC line boundary. As such, the reliability and precision of the final fault location results might be reduced. Therefore, in the next section, the backward traveling waves (BTWs) will be introduced and analyzed for fault location.

3.3. The time-domain expressions of backwards line-mode current TWs

As described in Fig. 3(a), we assume the direction of the forward traveling waves (FTWs) from the DC bus to the cable. In contrast, the direction of the BTWs is from the cable to the DC bus. According to detailed derivations provided in [22], the BTWs of voltage/current $v_{b(1)34}(s)$ and $i_{b(1)34}(s)$ can be calculated as:

$$\begin{cases} v_{b(1)34}(s) = \dfrac{v_{(1)34}(s) - Z_{c(1)}i_{(1)34}(s)}{2}, \\ i_{b(1)34}(s) = \dfrac{-v_{b(1)34}(s)}{Z_{c(1)}}. \end{cases} \tag{6}$$

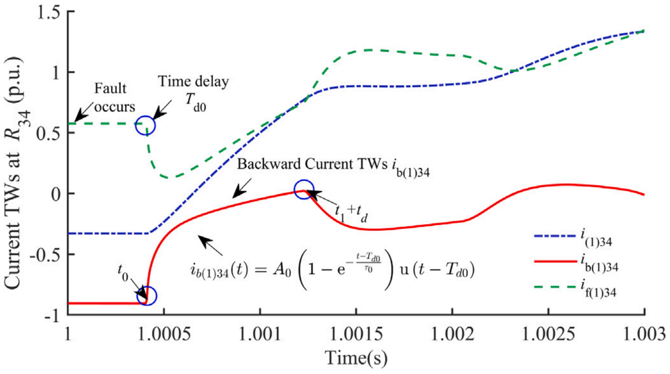

Fig. 4. Simulation of $i_{b(1)34}(t)$ in the testing system.

Combining (4) and (6), the expression of $i_{b(1)34}(s)$ with fault location l becomes:

$$\begin{aligned} i_{b(1)34}(s) &= \frac{Z_{c(1)}i_{(1)34}(s) - v_{(1)34}(s)}{2Z_{c(1)}} \\ &= \frac{\Delta v_{F1}}{sZ_{c(1)}}\frac{1-k_0 l}{1+s\tau l}\,\mathrm{e}^{-s\frac{l}{v_{(1)}}} = A_0\left(\frac{1}{s}-\frac{1}{s+1/\tau_0}\right)\mathrm{e}^{-sT_{d0}}. \end{aligned} \tag{7}$$

Using the *Inverse Laplace Transform*, we obtain the following time domain expression for $i_{b(1)34}(t)$:

$$i_{b(1)34}(t) = A_0\left(1-\mathrm{e}^{-\frac{t-T_{d0}}{\tau_0}}\right)\mathrm{u}\left(t-T_{d0}\right), \tag{8}$$

where, the function $u\left(t-T_{d0}\right)$ represents a step function with a time delay of $T_{d0} = l/v_{(1)}$. The values of A_0 and τ_0 can be calculated as:

$$A_0 = \frac{\Delta v_{F1}(1-k_0 l)}{Z_{c(1)}}, \qquad \tau_0 = \tau l. \tag{9}$$

where the values are $k_0 = 5.0\times10^{-5}$/km, and $\tau = 6.98275\times10^{-7}$s/km for the studied cable model.

The simulation of $i_{(1)34}(t)$, $i_{b(1)34}(t)$ and $i_{f(1)34}(t)$ can be seen in Fig. 4, assuming that the metallic ptg fault occurs at l_{34} with a fault location of 80 km. Since the wavefront of BTWs (waveform between the two blue circles) monitored at relay units is not refracted or reflected by the line boundaries, the $i_{b(1)34}(t)$ contains pure fault location information as the parameter A_0 and τ_0 are independently mapped to l. Thus, they are preferred objects for studying the initial fault characteristics and response and for fault location.

Similarly, the expression for the $i_{b(1)43}(t)$ measured at relay unit R_{43} can be expressed as:

$$i_{b(1)43}(t) = A'_0\left(1-e^{-\frac{t-T'_{d0}}{\tau'_0}}\right)\mathrm{u}\left(t-T'_{d0}\right), \tag{10}$$

where the values for A'_0, T'_{d0} and τ'_0 can be obtained by replacing l with $(L-l)$ in (9). L is the length of cable l_{34}.

According to (8) and (10), it is feasible to determine the fault location l once the values of A_0, τ_0 or A'_0, and τ'_0 can be obtained from the sampled data of $i_{b(1)34}(t)$ and $i_{b(1)43}(t)$.

4. Introduction of the AMLM-algorithm based fault location method

This section introduces the AMLM algorithm-based parameter fitting and the proposed fault location method.

4.1. AMLM-based parameter fitting

4.1.1. Fitting function

Define the merit function as:

$$\min_{x\in R^2} \|H(x)\|^2 \tag{11}$$

Taking $i_{b(1)34}(t)$ as an example, the error function for parameter fitting is:

$$H(x) = i_{b(1)34} - A_0\left(1 - \mathrm{e}^{-\frac{t-T_{d0}}{\tau_0}}\right) \tag{12}$$

Here x is a two dimensional vector: $x = [A_0, \tau_0]_{1\times 2}$.

4.1.2. Adaptive multi-step levenberg–marquardt algorithm

To solve the nonlinear least-squares problems in (11), this work adopts the AMLM algorithm [23], which significantly reduces the number of iteration steps to converge to the optimal solution compared to the classic Levenberg–Marquardt (LM) algorithm in [24,25].

The iterate x_k using the AMLM algorithm is computed by:

$$x_{k+1} = \begin{cases} x_k + \delta_k, & \text{if } r_k = \frac{\|H_k\|^2 - \|H(x_k+\delta_k)\|^2}{\|H_k\|^2 - \|H_k + M_k\delta_k\|^2} \geq p_0, \\ x_k, & \text{otherwise,} \end{cases} \tag{13}$$

In (13), the criteria $r_k \geq p_0$ controls the adaptive step size δ_k at the kth iteration during iterations. p_0 is a small positive value set as 0.0001. The δ_k in (13) is determined as:

$$\delta_k = \frac{-M_k^T H_k}{\left(M_k^T M_k + \lambda_k I\right)}, \tag{14}$$

where I is an 2×2 identity matrix. λ_k is the LM parameter and is calculated by:

$$\lambda_{k+1} = \begin{cases} \lambda_k, & \text{if } r_k \geq p_1 \text{ and } s < \mu, \\ \beta_{k+1}\left\|H_{k+1}\right\|^{\delta}, & \text{otherwise,} \end{cases} \tag{15}$$

where

$$\beta_{k+1} = \begin{cases} c_1\beta_k, & \text{if } r_k < p_2, \\ \beta_k, & \text{if } p_2 \leq r_k \leq p_3, \\ \max\left\{c_2\beta_k, \beta_{\min}\right\}, & \text{if } r_k > p_3. \end{cases} \tag{16}$$

The M_k is the Jacobian J_k, which is $\left[-1 + \mathrm{e}^{-\frac{t}{\tau_0}}, \frac{A_0 t}{\tau_0^2}\mathrm{e}^{-\frac{t}{\tau_0}}\right]$, or the Jacobian used at the last step x_k:

$$M_{k+1} = \begin{cases} M_k, & \text{if } r_k \geq p_1 \text{ and } s < \mu, \\ J_{k+1}, & \text{otherwise,} \end{cases} \tag{17}$$

If the stop condition $\left\|M_k^T H_k\right\| \leq 10^{-5}$ is met, it shows that the algorithm converges superlinearly under a small tolerance, the solution at step k $x_k = [A_{0,k}, \tau_{0,k}]$ is optimal for (11) and the iteration is terminated. Otherwise, the algorithm continues to the next iteration. The parameter fitting for $i_{b(1)43}(t)$ can be achieved following the above procedures by replacing the l with $(L-l)$ in the error and merit function in (11)–(12).

Applying (14)–(17), the fault location method using the AMLM algorithm can be formulated as the following **Algorithm** 1.

4.2. Single-ended fault location method

In Eqs. (8) and (10), it is shown that the indices A_0, τ_0 or A_0', and τ_0' contain information about the fault location l. However, deriving l directly in terms of A_0 or A_0' is complicated, as they are affected by the fault type and the fault resistance R_f according to Table 2. In contrast, the parameter τ_0 and τ_0' are solely associated with l, making it a preferred indicator for fault location.

Algorithm 1 The proposed fault location method using the adaptive multi-step Levenberg Marquardt algorithm

```
Require: Selected data $i_{b(1)34}$, $i_{b(1)43}$ by FEO
Require: $x_1 \in R^2, c_1 > 1 > c_2 > 0, 0 < p_0 < p_2 < p_1 < p_3 < 1, 1 \leq \delta \leq 2, t \geq 1, \beta_1 > \beta_{min} > 0$
Ensure: Set $G_1 = J_1$, $\lambda_1 = \beta_1 \left\|H_1\right\|^{\delta}$, $k = 1, s = 1, i = 1, k_i = 1$
  $p_0 \leftarrow 0.0001$, $p_1 \leftarrow 0.50$, $p_2 \leftarrow 0.25$, $p_3 \leftarrow 0.75$
  $c_1 \leftarrow 4.0$, $c_2 \leftarrow 0.25$,
  $\beta_1 \leftarrow 10^{-5}$, $\beta_{min} \leftarrow 10^{-8}$
  while $\left\|M_{k_i}^T H_{k_i}\right\| \neq 0$ do
      $\delta_k \leftarrow -M_k^T H_k / \left(M_k^T M_k + \lambda_k I\right)$                ▷ (14)
      $\beta_{k+1} \leftarrow c_1$  or  $\beta_k$  or  $\max\left\{c_2\beta_k, \beta_{\min}\right\}$  ▷ (16)
      $\lambda_{k+1} \leftarrow \lambda_k$  or  $\beta_{k+1}\left\|H_{k+1}\right\|^{\delta}$          ▷ (15)
      $x_{k+1} \leftarrow x_k + \delta_k$                                    ▷ (13)
      if $r_k \geq p_1$ and $s < \mu$ at $x_k$ then                          ▷ (17)
          $M_{k+1} \leftarrow M_k$, $s = 1, i = i + 1, k_i = k$.
      else if Otherwise then
          $M_{k+1} \leftarrow J_k$, $s = s + 1$.
      end if
      if $\left\|M_k^T H_k\right\| \leq 10^{-5}$ then
          Terminate iteration                            ▷ $x_k$ is optimal for (11)
      else if $\left\|M_k^T H_k\right\| > 10^{-5}$ then
          $k = k + 1$
      end if
  end while
      Return $A_0$, $\tau_0$, $A_0'$, $\tau_0'$
```

As the DC fault in l_{34} is the internal fault for both relays R_{34} and R_{43}, the fault location can be determined either using the sampled data $i_{b(1)34}$ or $i_{b(1)43}$ (without data exchange between R_{34} and R_{43}). To ensure the accuracy of the fault location, we first fit the data of sampled $i_{b(1)34}$ and $i_{b(1)43}$. Then, it selects the data with higher R^2 values for subsequent fault locations. Here, the R^2 is an efficient index to evaluate the performance of the AMLM-based parameter fitting. The formula for R^2 is:

$$R^2 = 1 - \frac{SSR}{SST}, \tag{18}$$

where SSR denotes the sum of squared residuals, and SST is the total sum of squares. The $R^2 \in [0, 1]$, where a higher value indicates a better fit between fitted and simulated data.

As such, the estimated fault location l^* is:

$$l^* = \begin{cases} \frac{\tau_0}{\tau}, & \text{if } R_{34}^2 \geq R_{43}^2, \\ L - \frac{\tau_0'}{\tau}, & \text{otherwise,} \end{cases} \tag{19}$$

Using (19), the accuracy of fault location for close-in faults can be significantly enhanced. This is because the data measured at the far end of relays is closer to the theoretical expressions derived in (8) and (10) due to less attenuation over the traveling distance and fewer injections and reflections. Consequently, this data contains purer fault location information with a longer data window, allowing for better parameter fitting and resulting in more accurate fault location results.

4.3. Data window determination

To ensure that the selected data is as close as possible to (8) and (10), the data window is chosen from either $(t_0, t_1 + t_d)$ or $(t_0', t_1' + t_d)$ using the calculator FEO (Fenley Energy Operator) for parameter fitting. Here, t_0 and t_0' are the times when the fault-induced TWs arrive at the relay units R_{34} and R_{43} with time delays of T_{d0} and T_{d0}', respectively. The Values t_1 and t_1' are the times when $i_{b(1)34}(t)$ and $i_{b(1)43}(t)$ reach their peak values. Here, the FEO energy operator has the merits of detecting transients and frequency shifts in signals, which can be seen as

$$\phi_{feo}(s(n)) = s(n+1)^2 - s(n-1)s(n) + s(n-1)^2 - s(n)s(n+1), \tag{20}$$

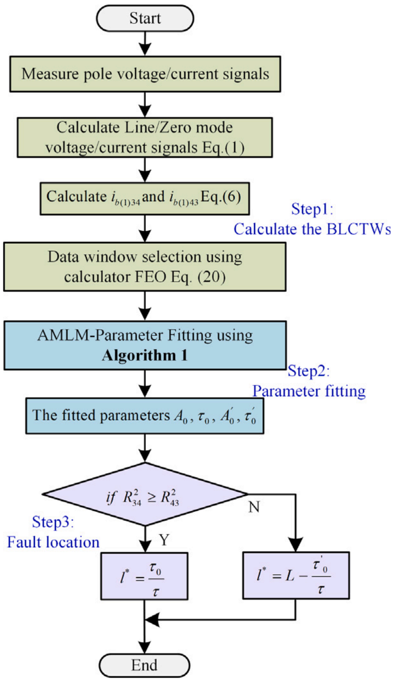

Fig. 5. The flowchart of the proposed fault location method.

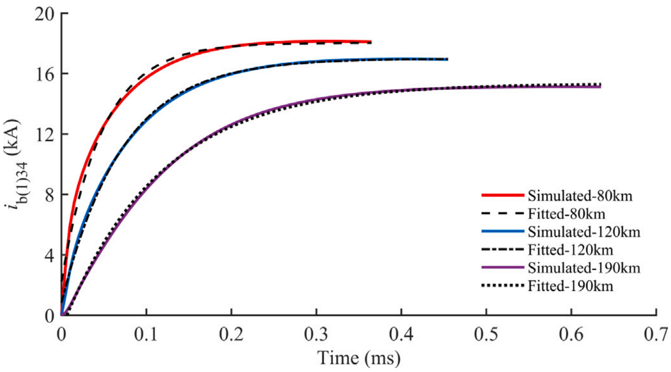

Fig. 6. Parameter fitting results for $i_{b(1)34}$ under ptp faults.

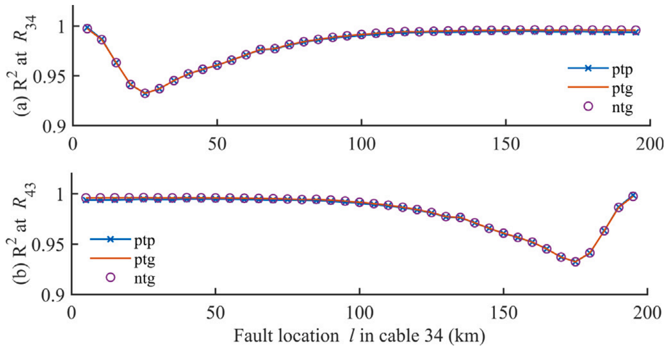

Fig. 7. Results evaluation of parameter fitting using R^2 values. (a) Results at relay R_{34}. (b) Results at relay R_{43}.

where the $\phi_{feo}(s(n))$ is the energy calculated by FEO used to select the data window; The $s(n)$ is the discrete data of $i_{b(1)34}$, $i_{b(1)43}$.

Value $t_d = 50\,\mu s$ is a short time window added to improve anti-noise interference ability. This value can be adjusted if a different sampling frequency is used and a different maximum noise level is considered; For the 200 kHz and 35 dB SNR noise investigated in the manuscript, $t_d = 50\,\mu s$ is tested as an optimal solution; if the value of t_d is increased, the selected data might not closely refer to the expressions in (8) and (10). If the value of t_d decreases, the anti-noise ability will be reduced. As such, $t_d = 50\,\mu s$ is a trade-off and is considered a fair solution considering the conditions in the studied system and fault conditions. For other testing systems, this value needs to be adjusted by different considerations; The general principle is: if the sampling frequency f_s is increased, the value of t_d should be decreased, otherwise additional data are added to the data window which does belong to the range of Eq. (8) and vice versa; if the noise level is increased, the value of t_d should be increased accordingly, otherwise noise will severely affect the identification of the data window's endpoint, especially in cases of close-in faults. The exact value of adjustment of t_d must be carefully designed based on numerous tests.

To evaluate the accuracy of the proposed fault location method in the following contents, the error is defined by:

$$e = \left| \frac{l - l^*}{L_{cable34}} \right| \%, \tag{21}$$

where $L_{cable34} = 200$ km.

To implement the proposed fault location in other testing systems, it is necessary to determine suitable initial values required in **Algorithm 1** and τ in (9) according to the previous analysis. The overall proposed fault location method can be seen in Fig. 5.

5. Simulation and discussion in PSCAD

The simulations are carried out in the PSCAD/EMTDC environment for the MMC-MTDC system shown in Fig. 1. All the faults are simulated at l_{34}. The data are measured from the relay units R_{34} and R_{43}. In practice, cable faults are commonly caused by metallic damage [1]. Due to this, the faults with large values of the R_f are not considered in this work. The sampling frequency $f_s = 200$ kHz in PSCAD/EMTDC was chosen for testing the method, which is technically possible to achieve in practice, e.g., the commercially available high-resolution relays SEL-T401L, SEL-T400L, and SEL-TWFL.

5.1. Fault location performance

Taking the ptp faults as examples, the parameter fitting results with different fault locations can be seen in Fig. 6. It is concluded that the fitted waveform of $i_{b(1)34}$ by the AMLM algorithm closely matches the simulated one, which proves the previous results (8) and the accuracy of the AMLM algorithm. Additional testing results evaluated using the R^2 are presented in Fig. 7. The fault locations range from 5 km to 195 km in l_{34} with a step of 5 km. Due to the Symmetrical system structure and the results shown previously in Table 2, the $i_{b(1)34}$ and $i_{b(1)43}$ under ptg and ntg faults are the same in theory. As such, the measured and fitted results shown in Fig. 7 are mostly overlapped. The results shown in Fig. 7 include 239 different fault scenarios, with the average and median values of R^2 are 0.98171 and 0.9937. Almost all the R^2 values at both sides are close to 1.0, indicating that the AMLM algorithm has successfully optimized the objective function in (12). The AMLM-based parameter fitting yields highly accurate indexes regardless of the fault location or fault type. Consequently, the fitted data can be used for estimating the fault location. The mapping relationship between τ_0 and τ_0' is reliable and precise.

Typical ptg and ptp faults are simulated to validate the proposed fault location method, and the results are given in Table 3. According to Table 3, the proposed method has well-estimated the fault locations. The fault location errors are less than 0.4% for all presented scenarios. These results confirm that the proposed method has a desirable TWs parameter fitting ability and is employable for fault location purposes.

Table 3
Results of the fault location method (Metallic fault).

Scenario	l^* (km)	e (%)	Scenario	l^* (km)	e (%)
ptg_4 km	3.5910	0.2045	ntg_55 km	55.8099	0.4050
ptg_30 km	29.9685	0.0157	ntg_60 km	60.9447	0.4724
ptg_35 km	35.0759	0.0379	ntg_80 km	80.8442	0.4221
ptg_40 km	40.1708	0.0854	ntg_120 km	119.1547	0.4226
ptg_45 km	45.4280	0.2140	ntg_145 km	144.2494	0.3753
ptg_50 km	49.9017	0.0491	ntg_150 km	149.3475	0.3263
ptg_80 km	80.7592	0.3798	ntg_160 km	159.8216	0.0892
ptg_90 km	89.9084	0.0457	ntg_165 km	164.9836	0.0082
ptg_110 km	110.1069	0.0534	ntg_170 km	170.4508	0.2254
ptg_120 km	119.1602	0.4199	ptp_30 km	29.8193	0.0903
ptg_150 km	150.1790	0.0894	ptp_40 km	40.4864	0.2431
ptg_160 km	159.8287	0.0857	ptp_50 km	49.6853	0.1573
ptg_165 km	164.9902	0.0049	ptp_60 km	60.5644	0.2822
ptg_170 km	169.9483	0.0258	ptp_80 km	80.555	0.2775
ntg_3 km	2.510	0.2450	ptp_120 km	119.4688	0.2656
ntg_30 km	29.5524	0.2238	ptp_140 km	139.4427	0.2786
ntg_35 km	35.0843	0.0421	ptp_150 km	150.2883	0.1441
ntg_40 km	40.1794	0.0897	ptp_160 km	159.4507	0.2746
ntg_45 km	45.4373	0.2187	ptp_170 km	170.1694	0.0846

5.2. Influence of boundary conditions

The DC inductor L_{dc}, acting as the boundary element, has an impact on the propagation process of TWs as it reflects voltage/current TWs when they arrive at the relay units and the final performance of fault location methods. Using the $i_{b(1)34}$ has the merit of avoiding this issue emerging in classical TWs-based methods as the wavefront of BLCTWs is not reflected at the boundary. This section investigates the influence of different values of the L_{dc} (strong or weak boundary conditions) on the proposed parameter fitting-based fault location method. Six independent DC faults with various sizes of L_{dc} are simulated in the tested system. Taking the fault f_{34}_ptg_110 km as an example, the parameter fitting results are shown in Fig. 8. Due to the different sizes of L_{dc}, the TWs of $i_{b(1)34}$ after faults and the data window used for parameter fitting vary accordingly. However, the applied AMLM fitting algorithm still performs well in all cases, as shown in Fig. 8.

Table 4 lists the corresponding fault location results. Since L_{dc} is a system parameter, the value of τ must be adjusted for parameter fitting when different values of L_{dc} are used. Specifically, for $L_{dc} \in \{20\text{ mH}, 60\text{ mH}, 80\text{ mH}, 100\text{ mH}\}$, $\tau \in \{5.559\times10^{-7}, 6.2383\times10^{-7}, 6.405\times10^{-7}, 6.6325\times10^{-7}\}$, respectively. The results demonstrate that, with a reasonable selection of τ values, the proposed method exhibits a high degree of independence from the size of L_{dc}. Moreover, the estimated error e exhibits only marginal changes in response to variations in the size of L_{dc}, remaining within an acceptable range. This also indicates that the proposed method can be flexibly applied to other MTDC systems with different boundary conditions and can be extended in conditions of DC protection algorithms that do not rely on boundary devices.

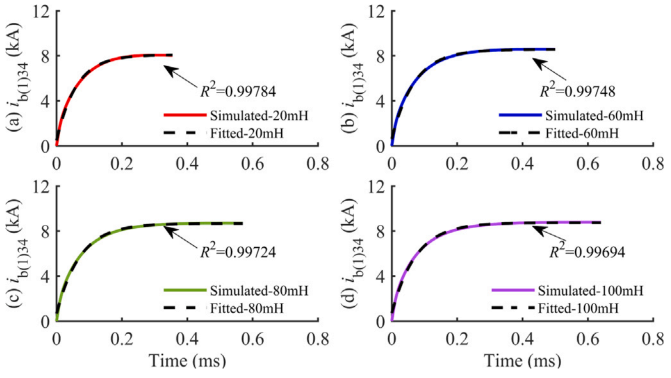

Fig. 8. Parameter fitting results for $i_{b(1)34}$ with various sizes of L_{dc}. (a) L_{dc} = 20 mH; (b) L_{dc} = 60 mH; (c) L_{dc} = 80 mH; (d) L_{dc} = 100 mH.

Table 4
Influence with different DC inductors.

Scenario	L_{dc} = 20 mH			L_{dc} = 60 mH		
	R^2	l^* (km)	e (%)	R^2	l^* (km)	e (%)
ptg_50 km	0.99943	49.1671	0.4164	0.99988	50.2065	0.1032
ptg_110 km	0.99784	109.6796	0.1602	0.99748	110.7108	0.3554
ptg_150 km	0.99943	150.8419	0.4209	0.99988	149.8727	0.0636
ptp_80 km	0.99875	80.7125	0.3563	0.99848	79.9116	0.0442
ptp_140 km	0.99958	139.5485	0.2258	0.99973	139.5749	0.2125
ptp_170 km	0.99903	170.4169	0.2084	0.99985	169.8425	0.0788
Scenario	L_{dc} = 80 mH			L_{dc} = 100 mH		
	R^2	l^* (km)	e (%)	R^2	l^* (km)	e (%)
ptg_50 km	0.99986	49.9345	0.0328	0.99977	49.8645	0.0678
ptg_110 km	0.99724	110.7103	0.3552	0.99694	110.7833	0.3916
ptg_150 km	0.99986	150.1212	0.0606	0.99785	149.8734	0.0633
ptp_80 km	0.99825	80.0269	0.0135	0.99793	79.7753	0.1124
ptp_140 km	0.99958	139.548	0.2260	0.99928	139.9985	0.0007
ptp_170 km	0.99991	170.0706	0.0353	0.99969	170.2024	0.2024

5.3. Noise effects

The measured voltage or current may contain noise from the CT and PT during measurement or when the power systems operate under abnormal conditions, such as load changing or control switching. To ensure the simulation environment reflects real conditions more accurately, this section introduces signal-to-noise ratios (SNR) of various noise levels in the MTDC system to test the anti-noise ability of the proposed method. The AMLM-based parameter fitting and fault locations results are given in Fig. 9 and Table 5. According to Fig. 9, the parameter fitting is minimally affected by noise interference, and the waveform of $i_{b(1)34}(t)$ can be well fitted with the R_2 values of 0.99754 and 0.99879, respectively. As the noise is stochastic, this paper repeated each set of noise tests 50 times. The results, e.g., R^2, l^* and e in Table 5, are all averaged values. As expected, the noise impacts the performance compared with the results in Table 5. This is because the noise may affect the selected data window, reducing the R^2 of parameter fittings. The largest error is 1.3965% when the ptp_60 km fault occurs. Overall, the fault location results under noise are accurate as all the estimated errors are smaller than 0.7%, indicating that the proposed method has a tolerance to noise up to 35 dB. When the noise level is up to 30 dB, the performance of the proposed fault location method is significantly reduced. Compared to the methods developed in [26–29], this method exhibits improved anti-noise ability. It is worth noting that when there are higher noise levels in the measurements (i.e., SNR less than 35 dB), the DC fault location becomes more challenging, particularly for close-in faults. However, such situations are quite rare in real environments. Therefore, the proposed method has enough anti-interference ability to be implemented in real projects. Further work will be continued to enhance the anti-noise ability of the proposed method.

Table 5
Fault location results under different noise levels.

Noise level	No noise	50 dB	45 dB	40 dB	35 dB	30 dB
Avg errors (%)	0.2139	0.2542	0.3689	0.4339	0.6575	1.8956
Max errors (%)	0.5687	0.6259	0.7853	0.8564	1.3965	2.5436
Avg R^2	0.99987	0.99875	0.99842	0.99736	0.98642	0.97826

5.4. Performance with lower sampling frequencies

Here, six metallic faults are performed to investigate the performance with lower sampling frequencies. According to the R^2 values in Table 6, the adopted AMLM **Algorithm** 1 can still optimize (11)

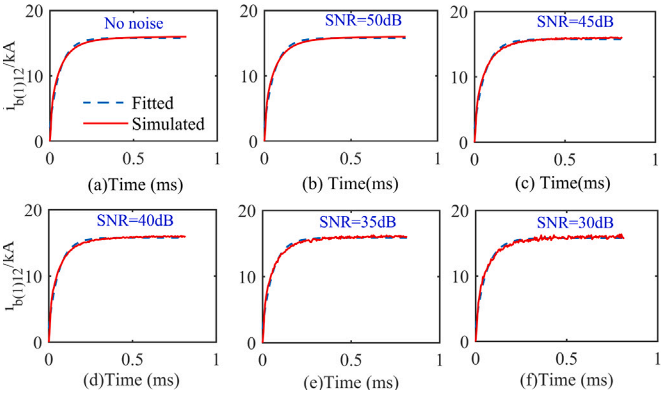

Fig. 9. Parameter fitting under fault f_{34}_ptg_80 km: (a) No noise; (b) SNR = 50 dB; (c) SNR = 45 dB; (d) SNR = 40 dB; (e) SNR = 35 dB; (f) SNR = 30 dB.

Table 6
Influence with lower sampling frequency f_s.

Scenario	$f_s = 50$ kHz			$f_s = 20$ kHz		
	R^2	l^* (km)	e (%)	R^2	l^* (km)	e (%)
ptg_130 km	0.99929	128.1488	0.9256	0.99992	132.0088	1.0044
ptg_140 km	0.99978	140.1209	0.0604	0.99993	139.9478	0.0261
ptg_150 km	0.99982	151.1544	0.5772	0.99994	147.0590	1.4705
ptp_110 km	0.99691	107.2704	1.3648	0.99991	112.2724	1.1362
ptp_120 km	0.99958	125.4541	2.7271	0.99995	119.5548	0.2226
ptp_130 km	0.99930	130.0928	0.0928	0.99997	125.5855	2.2073

to obtain the corresponding indexes for fitted TWs curve well for lower f_s. However, the accuracy of parameter fitting and fault location are influenced compared to the results in Table 3. This is due to a significantly reduced data window with a lower sampling frequency affecting the accuracy of fitted values of τ_0 and τ_0'. Taking the fault ptg_140 km as an example, the number of discrete sampling data used for AMLM parameter fitting is 9 and 23 under f_s being 20 kHz and 50 kHz, respectively. However, when the f_s is 200 kHz, the number of data that can be utilized jumps to 90. To guarantee accuracy and reliability and reduce the range of 'dead zone,' the lowest sampling frequency for the proposed method, based on numerous tests, is 20 kHz. More research is needed in future to improve the performance under lower f_s, e.g., 10 kHz.

6. RTDS experimental validation

This section evaluates the proposed fault location method within the RTDS environment.

6.1. Test system in RTDS

A ±525 kV three-terminal MMC-HVDC system depicted in Fig. 10 is modeled in detail in RTDS. The MMC is modeled using the most detailed model requiring three Xilinx Virtex-21 FPGA boards (GTFPGA) for one MMC unit. Two NovaCor racks, each with seven cores, are required for the system in Fig. 10. Cross-rack communication is achieved via a global bus hub and an IRC switch. The racks are connected to the GTFPGA units via the GTIO port, with signal exchanges facilitated by two full-duplex fiber optic cables using the standard high-speed Aurora protocol. The real-time wind speeds from the North Sea are extracted using the *Selenium* tool in a software-in-the-loop (SIL) configuration. The online wind data is communicated to RSCAD via a TCP/IP connection, with a communication delay of 100 ms, and data updates every 2 s. More detailed RTDS system descriptions, protection settings, and control allocations are discussed in [22,30,31].

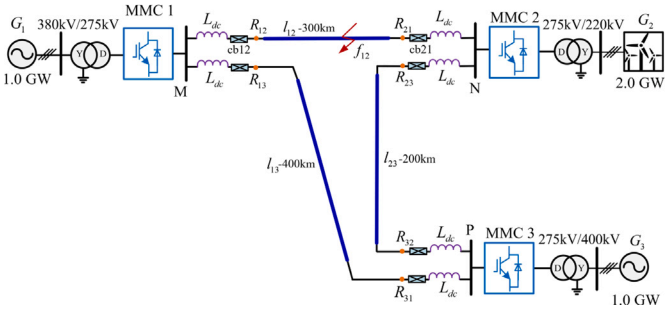

Fig. 10. Configuration of the ±525 kV MTDC system in RTDS.

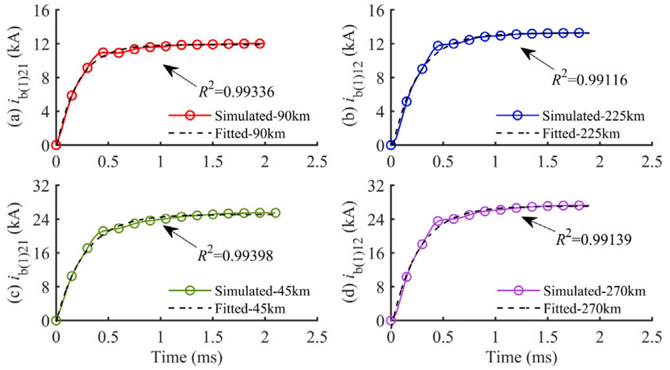

Fig. 11. Parameter fitting results for $i_{b(1)34}$ under faults: (a) ptg_90 km; (b) ptg_225 km; (c) ptp_45 km; (d) ptp_270 km.

6.2. Experimental fault location results

Cable l_{12} in Fig. 10 is the studied cable. The cable length is 300 km. Typical DC faults of different fault locations and fault types are used to test the performance of the proposed fault location method. The main time step in RTDS is 50 μs, and the sampling frequency is 20 kHz. The value of τ is 1.0255×10^{-6} in the studied system in Fig. 10. All the DC faults are metallic. Additional noise tests (each test is repeated 50 times) at 35 dB level are performed to validate the anti-noise capability in the RTDS environment.

The obtained results of the parameter fitting and detailed fault location are presented in Fig. 11 and Table 7, respectively. It can be observed from Fig. 11 that the proposed AMLM algorithm accurately fits the sampled TWs at relays R_{12} and R_{21}, with R^2 values approaching 1.0. Thus, the obtained indices provide sufficiently accurate estimates for the fault location. The results are shown in Table 7 and demonstrate that the proposed method accurately estimates the fault location in both normal and noisy environments, with errors within 1.0%. Although the accuracy slightly decreases compared to Table 3 in certain scenarios, it should be noted that this is due to the limitations of parameter fitting caused by a sampling frequency of 20 kHz. Overall, the results are presented in Table 7 still yields satisfactory outcomes for the proposed method.

7. Comparative analysis

The proposed method is thoroughly compared to other TWs-based fault location methods.

7.1. Compared to TW velocity-dependent methods

Apart from the above-compared methods, almost all the previous methods require the value of TW propagation velocity, which acts as a key factor affecting the fault location accuracy. In [32], the TWs

Table 7
Fault location results in RTDS environment (Metallic fault).

Scenario	Normal			SNR=35 dB		
	R^2	l^* (km)	$e(\%)$	R^2	l^* (km)	$e(\%)$
*ptg*_200 km	0.99354	199.5236	0.2382	0.99091	201.2945	0.6472
*ptg*_210 km	0.99375	208.3584	0.8208	0.99087	209.8657	0.0672
*ptg*_220 km	0.99349	219.4096	0.2952	0.99386	219.8608	0.0696
*ptp*_200 km	0.99228	198.2448	0.8776	0.99269	198.8083	0.5958
*ptp*_210 km	0.99232	208.1911	0.9044	0.9912	208.9830	0.5085
*ptp*_220 km	0.99216	219.0346	0.4827	0.9918	219.7597	0.1202
*ptp*_230 km	0.9920	230.0341	0.0170	0.99235	230.1496	0.0748
*ptp*_240 km	0.9916	241.6480	0.8240	0.99073	240.9215	0.4607

velocity is represented by a mathematical function that is fitted to simulated and/or actual fault data to obtain a more accurate velocity estimation. In [33], the TW velocity is estimated by setting a fault at the T1 node with a distance of 60 km. The initial TWs arrival time at terminal M1 is 2.015×10^{-4} s. Then, the velocity is determined to be 297.76 km/ms. In [26], the TW velocity is set to 183.5 km/ms using empirical knowledge. The method in [15] designed the TW velocity as a frequency-dependent variable, calculated using the frequency of the maximum IMF. In [34], an iterative-based modification equation is used to correct the velocity spectrum for different line segments. In [17], the velocities at terminal M and N are found to be $v_m = 299.220$ km/ms and $v_n = 299.184$ km/ms respectively by analyzing the modified frequency spectrums. In [29,35], the velocity is directly treated as fixed at 295.0 km/ms and 300 km/ms, respectively. Although these methods propose various approaches to estimate the velocity of TWs propagation for fault location, the TWs velocity in real projects is determined by various factors such as the conductor material, insulating medium, environmental conditions, transmission line structure, frequency, and load levels. As such, it is not an absolute constant value. The uncertainty of the velocity makes a significant impact on fault location accuracy.

In comparison, the proposed fault location method utilizes the fitted parameters τ and τ' from BLCTWs obtaining desired fault location results, which eliminates the necessity of estimating the TW velocity and the unreliability and low accuracy caused by inaccurate estimation of the TW velocity.

7.2. Compared to other TWs-based methods

To prominent the performance of the proposed method, this section provides the comparison study with the existing TWs-based fault location methods.

The authors in [17] introduced a TWFL method and the fault location l_1^* is set as:

$$l^* = \frac{v_{(1)Mtw} v_{(1)Ntw} (t_{M1} - t_{N1}) + v_{(1)Mtw} l_{12}}{v_{(1)Mtw} + v_{(1)Ntw}}, \tag{22}$$

where in [17], the line-mode TWs velocities at terminal M and N $v_{(1)Mtw}$ and $v_{(1)Ntw}$ are identified as 196.0784 km/ms and 196.3350 km/ms, respectively.

In [16,35], the first and second voltage TWs peaks at single side are used to reflect to the TWs arrival time. The fault location can be expressed as:

$$l^* = \frac{v_{(1)tw} \times (T_{s2} - T_{s1})}{2} \tag{23}$$

where $v_{(1)tw}$ is the TWs velocity at line-mode network; T_{s2} and T_{s1} are the second and first peak value timings of voltage magnitude.

It is evident that methods in [16,17,35] are dependent of TWs velocities, the precise estimation of $v_{(1)tw}$, $v_{(1)Mtw}$ and $v_{(1)Ntw}$ are needed. Besides, another key to TWFL1 and TWFL2 is the precise identification of t_{M1} and t_{N1}, which is determined using the S-transform in [17], DWT in [35] ('Haar' wavelet as mother wavelet and decomposition level is 2) and SVMD-TEO in [16];

Table 8
Comparisons with existing TWs methods.

Method	5 km	10 km	20 km	30 km	60 km	70 km
Proposed	5.12	9.86	19.75	29.97	59.78	69.34
S-Transform [17]	7.26	8.89	19.45	29.87	59.41	69.10
DWT [35]	3.13	7.98	19.56	28.97	60.45	71.23
SVMD-TEO [16]	4.19	11.45	20.03	29.74	60.78	69.09
Method	**90 km**	**100 km**	**110 km**	**120 km**	**130 km**	**150 km**
Proposed	89.91	99.45	110.11	119.16	129.35	150.18
S-Transform [17]	89.56	99.67	110.78	118.89	129.12	149.67
DWT [35]	89.79	98.56	109.45	121.01	129.08	149.02
SVMD-TEO [16]	89.23	98.79	108.79	119.12	127.76	148.47

For comparison studies, all the faults are metallic ptg faults set at l_{12} in Fig. 1 using a same f_s 200 kHz. The comparison results can be seen in Table 8 by reproducing the fault location algorithms in the same testing condition in [16,17,35] among the proposed method.

According to the results presented in Table 8, the proposed method provides more accurate fault location results compared to other methods. It is important to note that the methods in [16,17,35] use different time–frequency analysis tools to extract the high-frequency components contained in the faulty traveling waves (TWs), generated by the boundary element at the line terminal. The peak values in the frequency spectrum are mapped to the TWs' arrival times at the relays. However, the performance of these tools, especially their time–frequency resolution, is limited by the sampling frequency. When using a reduced value of f_s (compared to the values in [16,17,35]), the TWs' arrival times cannot be precisely identified, which consequently affects the accuracy of the fault location results. This drawback becomes more pronounced in close-in faults, such as the 5 km case shown in Table 8, where the available data is further reduced. All these limitations inherent in the classical methods [16,17,35] are mitigated by the proposed method through the use of fitted parameters for fault location.

7.3. Compared to other fault location methods

In this part, the proposed method is further compared to other methods using indexes such as sampling frequency (SF), Noise Withstand Ability (NWA), Synchronization (Sync), Close-in faults accuracy (CIFA), and Computational Complexity (CC), Real-time testing (RTT). The compared methods include the MMGA-based method in [28], the SAE-based method in [29], the CWT-based method in [27], and the SVMD-TEO-based method in [16]. The comparison results can be seen in Table 9.

The MMGA algorithm in [28] is applied to detect the first two wavefronts of voltage TWs by measuring the geometric characteristics. However, the accuracy of this method is significantly reduced under close-in faults. As reported, 4.39 km is estimated when the real location is 2 km (2390 meter error), which is caused by the low signal decomposition resolution of MMGA. This limitation is addressed in the proposed method. In [29], a 20 μs data window with 100 samples is collected as inputs for the stacked auto-encoder (SAE), which utilizes a 5 MHz for sampling. Similar issues are also exposed in the CWT-based method in [27] which uses a 2 MHz sampling to capture the wavefronts using the CWT coefficients, and the SVMD-TEO-based method in [16] which adopts an 1 MHz sampling rate to decompose the IMFs contained in the TWs. The EMD is used in [13] for measuring the 1st mode of IMF, multi-wavefronts are needed to obtain the fault location. The complex logic under various fault conditions and synchronization errors will reduce the accuracy under close-in faults and may limit the real applications. Similar to [15], the EMD also requires a high sampling rate (500 kHz in [13]) to obtain accurate IMFs. Besides, the performance under close-in faults is reduced, as the wavefronts are challenging to identify due to frequent injections/refractions of short propagation distance.

The real-time testing of these methods using a 50 μs simulation step (20 kHz sampling) needs further investigation, as the performance of

Table 9
Comparisons with other fault location methods.

Method in	[28]	[29]	[27]	[16]	[13]	Proposed
SF (kHz)	200	5000	2000	1000	500	200
NWA	50 dB	60dB	–	30dB	–	35 dB
Sync	No	No	Yes	Yes	Yes	No
CIFA	Low	Low	Low	Low	Low	High
RTT	No	No	No	No	No	Yes

these methods on a real-time simulation platform, in terms of reliability and accuracy, has not been tested or validated, and their potential and feasibility in practical applications cannot be guaranteed. In comparison, the proposed method exhibits comprehensive advantages under these compared methods.

8. Conclusion

This article proposes a new single-ended DC fault location method based on backward line-mode current TWs for the MTDC power system. Firstly, it is derived that the backward line-mode current TWs can be approximated to an exponential function with a parameter containing the fault location. Then, the AMLM algorithm is used for parameter fitting. The calculating procedure of the AMLM algorithm is elaborated. Finally, the performance validation of the proposed method is done via PSCAD/EMTDC and RTDS platforms.

According to the results, the proposed parameter fitting algorithm and fault location method are accurate, with all the R^2 values close to 1.0 (perfect fitting), and most errors are smaller than 0.5%. It also performs excellently with different sizes of DC inductors. The method does not require a high sampling frequency and communication channel, significantly reducing the hardware requirements and investment in practical applications. The authors also investigated noise tests. The presented results confirm the superiority of the proposed fault location method in withstanding the 35 dB noises. Additionally, by comparing the R^2 values of the fitted BLCTWs, the optimal coefficients from the sampled and fitted BLCTWs are used for fault location, which significantly enhances the reliability and accuracy of fault location under close-in faults.

This work can be extended in the following directions: (1) Enhancing the method's anti-noise ability to resist higher noise levels (SNR $\leq$ 35 dB); (2) Implementing the proposed fault location method in the FPGA units and conducting hardware-in-the-loop (HIL) testing using RTDS; (3) Extend the proposed method to apply to overhead and cable/overhead hybrid transmission lines. (4). Considering the impact of nonlinear fault resistance to the fault analysis and fault location performance;

CRediT authorship contribution statement

Le Liu: Writing – original draft, Visualization, Validation, Software, Methodology, Investigation, Formal analysis, Data curation. **Fan Xie:** Investigation, Formal analysis, Data curation, Conceptualization. **Xiaoning Kang:** Writing – review & editing, Supervision. **Zhiguo Hao:** Writing – review & editing, Supervision. **Aleksandra Lekić:** Writing – review & editing, Supervision, Investigation. **Marjan Popov:** Writing – review & editing, Supervision, Investigation, Conceptualization.

Declaration of competing interest

The authors declare that they have no known competing financial interests or personal relationships that could have appeared to influence the work reported in this paper.

Acknowledgment

The first two authors thank TU Delft for providing opportunities to conduct this research at the Delft University of Technology in the framework of the CSC program.

Data availability

No data was used for the research described in the article.

References

[1] Liu L, Liu Z, Popov M, Palensky P, van der Meijden MAMM. A fast protection of multi-terminal HVDC system based on transient signal detection. IEEE Trans Power Deliv 2021;36(1):43–51.
[2] Liu L, Kang X, Ma X, Chen X, Li S, Li X, Liu X. MPLM algorithm based fault location method for MTDC systems using backward voltage traveling waves. Electr Power Syst Res 2024;235:110880.
[3] He Z-Y, Liao K, Li X-P, Lin S, Yang J-W, Mai R-K. Natural frequency-based line fault location in HVDC lines. IEEE Trans Power Deliv 2013;29(2):851–9.
[4] He J, Li B, Sun Q, Li Y, Lyu H, Wang W, Xie Z. The improved fault location method based on natural frequency in MMC-HVDC grid by combining FFT and MUSIC algorithms. Int J Electr Power Energy Syst 2022;137:107816.
[5] Xu J, lü Y, Zhao C, Liang J. A model-based DC fault location scheme for multi-terminal MMC-hvdc systems using a simplified transmission line representation. IEEE Trans Power Deliv 2020;35(1):386–95. http://dx.doi.org/10.1109/TPWRD.2019.2932989.
[6] Song G, Yan J, Chang Z, Zhang C, Gao X. A frequency-domain fault location method for underground cables in MMC-hvdc systems. IEEE Trans Instrum Meas 2024;73:1–12.
[7] Song G, Hou J, Guo B, Wang T, Masood B, Kazmi STH. Single-ended active injection for fault location in hybrid MMC-hvdc systems. Int J Electr Power Energy Syst 2021;124:106344.
[8] Wang T, Song G, Hussain KST. Adaptive single-pole auto-reclosing scheme for hybrid MMC-hvdc systems. IEEE Trans Power Deliv 2019;34(6):2194–203.
[9] Elgamasy MM, Izzularab MA, Zhang X-P. Single-end based fault location method for VSC-HVDC transmission systems. IEEE Access 2022;10:43129–42.
[10] Yang Q, Le Blond S, Aggarwal R, Wang Y, Li J. New ANN method for multi-terminal HVDC protection relaying. Electr Power Syst Res 2017;148:192–201.
[11] Kanwal S, Jiriwibhakorn S. Advanced fault detection, classification, and localization in transmission lines: A comparative study of ANFIS, neural networks, and hybrid methods. IEEE Access 2024;12:49017–33.
[12] Panahi H, Sanaye-Pasand M, Niaki SHA, Zamani R. Fast low frequency fault location and section identification scheme for VSC-based multi-terminal HVDC systems. IEEE Trans Power Deliv 2021;37(3):2220–9.
[13] Wang J, Zhang Y. Traveling wave propagation characteristic-based LCC-mmc hybrid hvdc transmission line fault location method. IEEE Trans Power Deliv 2022;37(1):208–18. http://dx.doi.org/10.1109/TPWRD.2021.3055840.
[14] Javaid S, Li D, Ukil A. High pass filter based traveling wave method for fault location in VSC-interfaced HVDC system. Electr Power Syst Res 2024;228:110004.
[15] Zeng R, Zhang L, Wu Q-H. Fault location scheme for multi-terminal transmission line based on frequency-dependent traveling wave velocity and distance matrix. IEEE Trans Power Deliv 2023;38(6):3980–90.
[16] Zeng R, Wu Q, Zhang L. Two-terminal traveling wave fault location based on successive variational mode decomposition and frequency-dependent propagation velocity. Electr Power Syst Res 2022;213:108768.
[17] Wang D, Liu J, Hou M. Novel travelling wave fault location approach for overhead transmission lines. Int J Electr Power Energy Syst 2024;155:109617.
[18] Psaras V, Tzelepis D, Burt G. HVDC grid fault location method using genetic algorithm on reconstructed frequency-domain voltage profiles. Int J Electr Power Energy Syst 2023;144:108429.
[19] Cigré WG. B4. 57. "Guide for the Development of Models for HVDC Converters in a HVDC Grid". CIGRE Tech Brochure 2014;604.
[20] Liu L, Lekić A, Popov M. Robust traveling wave-based protection scheme for multiterminal dc grids. IEEE Trans Power Deliv 2023;1–13. http://dx.doi.org/10.1109/TPWRD.2023.3265748.
[21] Liu S, Popov M, Mirhosseini SS, Nee S, Modeer T, Angquist L, Belda N, Koreman K, van der Meijden MAMM. Modeling, experimental validation, and application of VARC hvdc circuit breakers. IEEE Trans Power Deliv 2020;35(3):1515–26.
[22] Liu L, Xie F, Popov M, Hao Z, Lekić A. Single-ended DC fault location method for MMC-based HVDC power system using adaptive multi-step levenberg-marquardt algorithm. In: IEEE PES PowerTech 2023. 2023.
[23] Fan J, Huang J, Pan J. An adaptive multi step levenberg marquardt method. J Sci Comput 2019;78(1):531–48.

[24] Zhang C, Li Y, Song G, Dong X. Fast and sensitive nonunit protection method for HVDC grids using Levenberg–Marquardt Algorithm. IEEE Trans Ind Electron 2021;69(9):9064–74.

[25] Zhang C, Song G, Meliopoulos AS, Dong X. Setting-less nonunit protection method for DC line faults in VSC-MTdc systems. IEEE Trans Ind Electron 2022;69(1):495–505. http://dx.doi.org/10.1109/TIE.2021.3050380.

[26] Farshad M, Karimi M. A signal segmentation approach to identify incident/reflected traveling waves for fault location in Half-Bridge MMC-HVdc Grids. IEEE Trans Instrum Meas 2022;71:1–9. http://dx.doi.org/10.1109/TIM.2021.3139688.

[27] Nanayakkara OMKK, Rajapakse AD, Wachal R. Traveling-wave-based line fault location in star-connected multiterminal HVDC systems. IEEE Trans Power Deliv 2012;27(4):2286–94. http://dx.doi.org/10.1109/TPWRD.2012.2202405.

[28] Yu X, Gu J, Zhang X, Mao J, Xiao L. A non-unit fault location scheme for MMC-HVDC grids based on the geometric features of the fault voltage. CSEE J Power Energy Syst 2024;1–13.

[29] Luo G, Yao C, Liu Y, Tan Y, He J, Wang K. Stacked auto-encoder based fault location in VSC-HVDC. IEEE Access 2018;6:33216–24.

[30] Liu L, Shetgaonkar A, Lekić A. Interoperability of classical and advanced controllers in MMC based MTDC power system. Int J Electr Power Energy Syst 2023;148:108980.

[31] Shetgaonkar A, Karmokar T, Popov M, Lekić A. Enhanced real-time multi-terminal HVDC power system benchmark models with performance evaluation strategies. CIGRE Science & Engineering 2024;32:1–29.

[32] Dardengo VP, Fardin JF, de Almeida MC. Single-terminal fault location in HVDC lines with accurate wave velocity estimation. Electr Power Syst Res 2021;194:107057.

[33] Zhu Y, Fan X. Fault location scheme for a multi-terminal transmission line based on current traveling waves. Int J Electr Power Energy Syst 2013;53:367–74.

[34] Yu D, Zhou N, Liao J, Wang Q, Lyu Y. Modified VMD algorithm-based fault location method for overhead-cable hybrid transmission line in MTDC system. IEEE Trans Instrum Meas 2024;73:1–11.

[35] Fayazi M, Joorabian M, Saffarian A, Monadi M. A single-ended traveling wave based fault location method using DWT in hybrid parallel HVAC/HVDC overhead transmission lines on the same tower. Electr Power Syst Res 2023;220:109302.